Plasma Sources
Science and
Technology

Effects of magnetic nozzle strength and orientation on radio-frequency plasma expansion

To cite this article: A Caldarelli *et al* 2023 *Plasma Sources Sci. Technol.* **32** 075002

OPEN ACCESS
IOP Publishing
Plasma Sources Science and Technology
Plasma Sources Sci. Technol. **32** (2023) 075002 (13pp)
https://doi.org/10.1088/1361-6595/ace1a6

Effects of magnetic nozzle strength and orientation on radio-frequency plasma expansion

A Caldarelli[1,*], **F Filleul**[1], **C Charles**[2], **R W Boswell**[2], **J E Cater**[3] **and N Rattenbury**[1]

[1] Department of Physics, The University of Auckland, 38 Princes Street, 1010 Auckland, New Zealand
[2] Space Plasma, Power and Propulsion Laboratory, Research School of Physics, The Australian National University, Canberra, ACT 2601, Australia
[3] Department of Mechanical Engineering, University of Canterbury, Christchurch 8140, New Zealand

E-mail: antonella.caldarelli@auckland.ac.nz

Received 23 March 2023, revised 19 June 2023
Accepted for publication 26 June 2023
Published 7 July 2023

Abstract

To improve the efficiency of radio-frequency magnetic nozzle plasma thrusters, it is important to better understand the coupling between plasma expansion and a convergent–divergent magnetic field. This study explores the effects of magnetic field strength and orientation on plasma expansion in a magnetic nozzle. Two-dimensional measurements of the plasma characteristics obtained both in the source and in the expansion region are presented to investigate the influence of magnetic field strength on the formation of high-density conics in a symmetric magnetic nozzle. The measurements are repeated in a deflected magnetic nozzle using a novel magnetic steering system. Measurements of the ion saturation current and floating potential profiles are used respectively to qualitatively assess the plasma density distribution and the presence of high-energy electrons for the magnetic field configurations analysed. In the symmetric magnetic nozzle configuration, it is observed that the ion saturation current peaks on axis in the plasma source, but downstream of the nozzle throat, a double-peaked hollow profile is observed for all cases studied. The location of the high-density conics structure matches the most radial field lines that intersect the antenna and can freely expand downstream outside the source. Negative values of the floating potential are measured in the same peripheral regions, which could be a sign of the presence of high-energy electrons. When the magnetic field is deflected, the ion saturation current profile shows only a single peak centred around the bent field line that reconnects to the antenna. Again, a region of negative floating potential is measured at the location of the maximum ion current. Thus, it is shown how, independent of magnetic field strength and orientation, the magnetic field lines interacting with the antenna dictate the local plasma profiles downstream from the magnetic nozzle.

---

[*] Author to whom any correspondence should be addressed.

1361-6595/23/075002+13$33.00 Printed in the UK

Keywords: magnetic nozzle, RF plasma, plasma expansion, high-density conics, magnetic steering

(Some figures may appear in colour only in the online journal)

---

1. Introduction

During the last two decades, radio-frequency (RF) low-temperature plasmas expanding in a convergent–divergent magnetic field (i.e. a magnetic nozzle) have been of particular attraction in the electric propulsion community due to the lack of electrodes and a neutraliser. Magnetised expanding plasmas are also of interest for research in plasma processing applications [1] and astrophysics [2, 3]. With the first measurement of the spontaneous generation of an accelerated ion beam via a current-free double layer in a helicon source [4] and the subsequent development of the helicon double layer thruster concept [5], efforts have been made to develop the technology [6–11]. Nevertheless, when examined with current state-of-the-art electric propulsion systems, the performance of magnetic nozzle RF plasma thrusters is still too low to make them a competitive alternative. The highest thruster efficiency obtained in an experimental campaign was reported by [12], who measured a 30% efficiency by placing a cusp magnetic field inside the plasma source to reduce wall losses.

Numerous experiments and simulations have reported the formation of a hollow density structure, also called high-density conics, in the diffusion region of an RF plasma expanding in a symmetric magnetic nozzle [13–24]. A common feature in the literature is the concomitance of the conics with the most radial streamlines leaving the source. The generation of these high-density conics has been attributed to high-energy electrons created a few skin depths under the antenna that escape the plasma source along the last radial field lines leaving the glass tube and causing off-axis local ionisation [15, 16, 19, 22, 24, 25]. Takahashi *et al* [16] have shown the presence of a high electron temperature region all along the field lines which intersect the antenna and can expand downstream. This free high-energy population was considered responsible for creating the hollow density structure. It was also observed that when the peripheral high-energy electrons present in the source were not permitted to move downstream, the high-density conical profile in the expansion region did not form [26]. As further proof, [18] observed that when the streamlines that reconnect to the antenna were not allowed to expand freely, the double-peaked feature would not occur. Additionally, [21] experimentally demonstrated that the high electron pressure conical profile contributes to the thrust generation, increasing the thrust along the axis of the magnetic nozzle. However, a complete understanding of the mechanisms that generate off-axis local ionisation is still unclear.

The concept of thrust vectoring via a steerable magnetic nozzle has also been the subject of different research campaigns [27–30]. This could allow for a mechanically simpler and more reliable orbit and attitude control mechanism since it does not comprise any moving or rotating components. It was noticed that the ion beam was effectively deflected as a result of applied transverse magnetic fields (TMFs), but that the magnetic field was not the dominant factor in controlling the ion beam deflection, as the latter was not following the orientation of the TMFs [27]. Thrust vector control by magnetic steering was experimentally demonstrated in two dimensions by mounting four additional solenoids after the plasma source exit [30]. Spatial mappings of the ion saturation current showed that the plasma plume was effectively deflected and that the high-density conics were still occurring. However, their profile was modified by the deflected MN.

To improve the efficiency of magnetised RF plasma thrusters, it is crucial for space propulsion and magnetic steering applications to fully understand the plasma expansion in a magnetic nozzle. Thus, further research on the formation of the hollow density profile and how a deflected magnetic field affects the plasma behaviour is required. The paper aims to study how the magnetic nozzle strength and orientation influence the local characteristics of the plasma during the expansion phase. Measurements are taken both in the plasma source and vacuum chamber to understand how the upstream conditions of the convergent–divergent magnetic field affect the downstream regions. While the design of RF magnetic nozzle plasma thrusters commonly include an antenna placed at the same axial location of the coils (i.e. the location of plasma excitation coincides with the magnetic nozzle throat), the experiments presented herein are conducted in an RF plasma device in which the antenna and the coils are not placed on the same axial location (see figure 3). Studies with a similar experimental design have been carried out by [16, 21, 29, 31–34]. In this configuration, the plasma is created remotely with respect to the magnetic nozzle throat. The study presents the first two-dimensional (2D) mappings in a RF plasma reactor, where the location of the plasma generation and the MN throat are decoupled, of the influence of magnetic field strength on the formation of the high-density conics, as well as the spatial characterisation of a deflected plasma plume with a novel steering system. Different magnetic field strengths and topology are used for this study: (a) a symmetric magnetic nozzle configuration with four different magnetic field strengths; and (b) a steered magnetic nozzle with a deflection angle with respect to the system axis of 15°. 2D measurements of the ion saturation current both in the plasma source and expansion chamber are presented to qualitatively assess the plasma density distribution for the magnetic nozzle configurations analysed. Contour plots of the floating potential measured in the divergent part of the magnetic nozzle are analysed to determine the peripheral presence of high-energy electrons, which are considered responsible for the enhanced off-axis ionisation. Additionally, plasma potential profiles are discussed to study the motion of the charged particles both on axis and radially.

It is observed that the magnetic field lines interacting in the source with the antenna affect the local plasma characteristics downstream of the magnetic nozzle, independent of magnetic field strength and orientation.

The work is organised as follows; section 2 describes the experimental set-up, including the plasma diagnostic probes and the data collection procedure. Section 3 discusses the measured data for the symmetric magnetic nozzle case with increasing field strength and for the deflected field configuration.

2. Apparatus and diagnostics

2.1. Apparatus

The experiments presented in this study are carried out in a RF magnetic nozzle plasma device at the University of Auckland called *Moa*. A sketch of the set-up and its main components is shown in figure 1(a). The plasma source is defined by a 150 cm long, 4.5 cm inner radius borosilicate glass tube, which connects through a custom-made vacuum flange to a 70 cm long, 25 cm radius steel vacuum chamber. The centre of the interface between the plasma source and the expansion chamber is defined as $(r,z) = (0,0)$ cm. A 1.3 turns loop antenna, centred at $z = -18$ cm, creates the plasma via an L-type matching network connected to a 1 kW RF power supply working at 27.12 MHz. A set of three skewed, concentric coils of increasing radius generate a convergent–divergent magnetic field of which intensity and orientation can be controlled by independently tuning the current input in each coil. Their design was based on the numerical study carried out by [28]. The coils are inclined of 15° with respect to the z axis and the system was designed to fit around the plasma source and be placed as close as possible to the glass tube/expansion chamber interface. The location of the magnetic nozzle throat is at $z = -8$ cm and the achievable magnetic field on axis is shown is figure 1(b) when all three coils are used. A section view of the magnetic system is shown in figure 3. A turbo pump with a pumping speed capability of 625 L s^{-1} for argon is used to reach a base pressure of $\sim 10^{-7}$ Torr, and a working pressure of ≈ 0.5 mTorr (70 MPa) is maintained throughout the experiments. The antenna and coils positions were set such that the magnetic field lines that intersect the antenna could freely escape the plasma source without intersecting any geometrical boundaries. This configuration allows for a better study of the RF skin layer-field lines coupling given the small and well-defined heating region.

2.2. Plasma diagnostics

The spatial mappings of the ion saturation current I_{sat} is carried out using an uncompensated planar Langmuir probe. Two different probes, with identical characteristics, are used to measure I_{sat}: one in the plasma source and one in the expansion chamber. The probes are constructed with a single-sided 2 mm diameter nickel disk biased at -100 V with respect to ground to ensure electron rejection. The collecting disks are attached to a 2 mm ceramic tube, which is in turn connected to a 6.35 mm stainless steel shaft. Floating potentials in the plasma source as negative as $-50/-70$ V have been measured in the apparatus, so a sufficiently negative biasing voltage is used to ensure that measurements are always performed in the ion saturation region. Since consistent results have been measured over a wide range of experimental conditions and studies, it is expected that the data collected do not to suffer from significant inaccuracies introduced by the value of V_{bias}. At each location, the reported I_{sat} is the average of the samples obtained from a data acquisition system with a sampling rate of 10^5 samples s^{-1} and a scan time of 1 s. Measurements taken at $-2 \leqslant z \leqslant 2$ cm with the two probes were compared to verify that both diagnostics were reporting accurate data. Due to the unavailability at the moment of the experimental campaign of an RF compensated Langmuir probe, reliable measurements of the electron temperature, and thus plasma density, could not be taken. Since the ion saturation current is proportional to the plasma density n_{p} and the square root of T_{e}, I_{sat} was used to qualitatively assess the profile of n_{p}. This approach has been used in other studies to infer the spatial distribution of the plasma density [18, 21, 29, 30, 35, 36]. The same probes are kept floating to measure the plasma floating potential V_{f}.

The emissive probe used in this study to measure the plasma potential V_{p} in the source consists of a U-shaped 0.127 mm diameter tungsten wire inserted into a 2 mm outer diameter, two bore ceramic tube and mounted on the same movable shaft as the Langmuir probe. A DC power supply, isolated from ground using an isolation transformer, is used to heat up the filament to allow thermionic emission. The respective *I*–*V* characteristic is found by sweeping the current from 1.5 to 2.6 A in steps of 0.025 A. The local plasma potential is obtained by using the floating method [37, 38], and the estimated measurement error is ±2.75 V.

A retarding field energy analyser (RFEA) is used in ion collection mode to measure the ion energy distribution function (IEDF) in the expansion chamber and to map the plasma potential. The design of the probe includes four nickel mesh grids (earth, repeller, discriminator and secondary electron grid) and a collector plate. The entrance orifice has a diameter of 2 mm and the probe head is mounted on a grounded 1/4′′ steel shaft. As the name suggests, the earth grid is kept at ground potential. The repeller is biased at -90 V to ensure electron rejection, while the discriminator grid is swept from $V_{\mathrm{D}} = 0 - 80$ V to filter the ions according to their energy. The secondary grid is biased at -18 V to repel secondary electrons caused by ion bombardment on the collector plate. The design of this probe is based on energy analysers extensively used in similar devices [6, 7, 19, 23, 39, 40]. The probe orifice is placed perpendicularly to the plasma source exit so that the presence of a directional ion beam could be detected. The biasing voltage of the RFEA is defined by several periods of a triangle wave function with a sweeping frequency of 10 Hz. Each measured current is the average of 200V_{D} sweeps. The collected current is fed into an analog differentiator to obtain the IEDF from the first derivative of the *I*–*V* characteristics [41]. The local plasma potential V_{p} and the ion beam potential V_{B} are then defined as the location of the first and second peaks in the IEDF [6, 10, 40, 42]. The error in the RFEA measurement for V_{p} is estimated to be ±2 V.

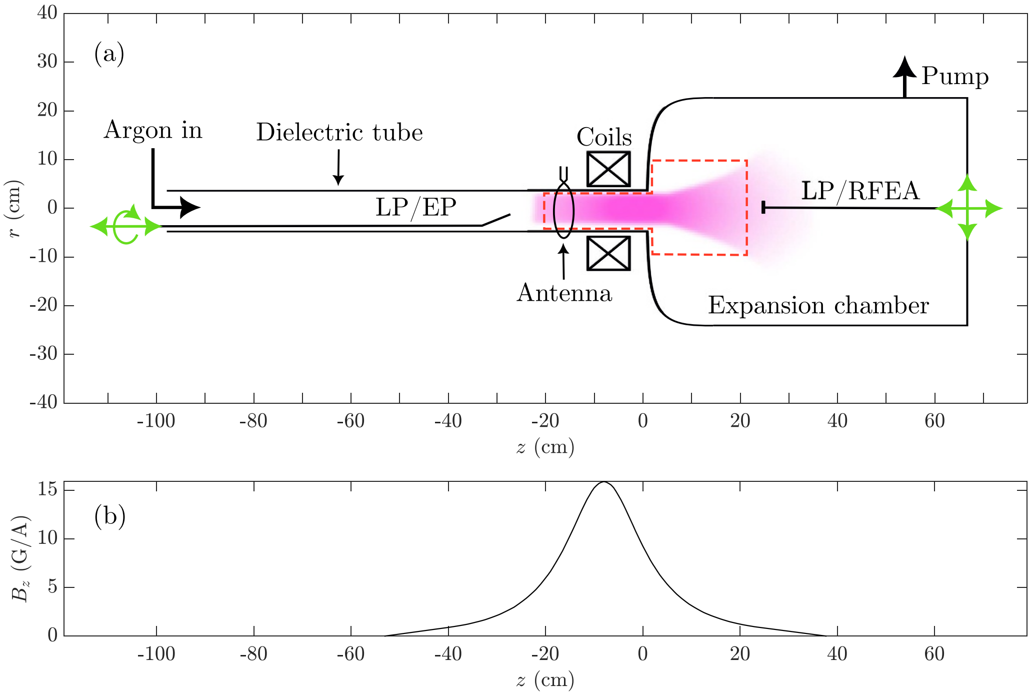

Figure 1. Schematic of the experimental set-up (a), and plot of the magnetic field on axis (b). The green arrows indicate the directions in which the probes can be moved. The dashed red boundary determines the region where measurements are taken.

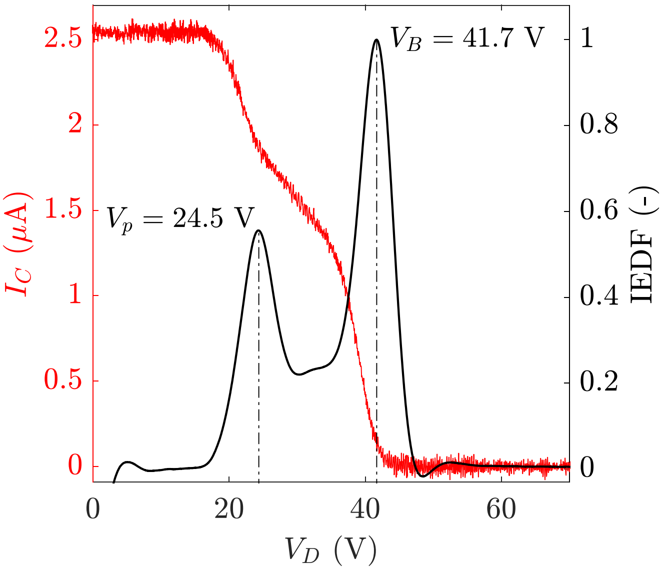

Figure 2. Example of an I–V curve (red line, left axis) and the ion energy distribution function (black line, right axis) measured at $(r, z) = (0, 13)$ cm by the RFEA.

Because the floating potential method could result in an inaccurate estimate of the plasma potential in RF plasmas [37], validation of the EP measurements was carried out by comparing the potentials obtained with values recorded with the RFEA. Figure 2 shows an example of an IEDF measured in the expansion chamber by the RFEA. As it can be seen, two distinct peaks are present. The first corresponds to the local plasma potential at $V_\mathrm{p} = 24.5\,\mathrm{V}$, while the second one corresponds to the potential of the ion beam, $V_\mathrm{B} = 41.7\,\mathrm{V}$. As it will be discussed in section 3, an ambipolar electric field is measured on axis that accelerates the ions created in the source. Thus, the value of V_B matches the value of plasma potential where the potential drop occurs. Table 1 summarises the maximum values of plasma potential measured by the EP in the plasma source (also shown in figure 6(a)) with the average ion beam potentials measured by the RFEA in the expansion chamber. The values show good agreement and are consistent with values for V_p and V_B reported in similar experiments [6, 10, 16, 17, 19, 29, 32, 40, 43–49].

Table 1. Comparison of maximum plasma potential $V_\mathrm{p,max}$ measured in the source with the EP and the average ion beam potential $V_\mathrm{B,avg}$ obtained with the RFEA in the expansion chamber. The values are all measured on axis.

$B_{z,\mathrm{max}}$ (G)	$V_\mathrm{p,max}$ (V)	$V_\mathrm{B,avg}$ (V)
77	48	49
120	50	50
175	45	46
330	42	41

2.3. Data acquisition

Spatial mappings of the plasma characteristics are obtained both in the plasma source and the expansion chamber. In the former, measurements are taken with the Langmuir probe and the emissive probe mounted on a movable (rotation and translation) doglegged eccentric steel shaft inserted on the left end of the experiment. The portion of the shaft in contact with the plasma is covered with a dielectric tube to minimise plasma perturbations. The angular and axial positions of the probes are controlled by two stepper motors. The shaft can be rotated of ±70° to move the probe tip from the centre to the edges of the glass tube ($r \approx 4.3$ cm). By taking advantage of the cylindrical symmetry of the plasma, spatial mappings in the source for the symmetric magnetic nozzle configuration are done by rotating the shaft of 10° increments on the θ–z plane. The measurements are then projected on the r–z plane. For the 2D measurements in the expansion chamber, the Langmuir probe and the RFEA are mounted on a movable 6.35 mm diameter steel shaft inserted in the right end of the experiment. A motorised rail system allows the probes to move along the axis, and a custom-made sliding vacuum feed-through mounted on a DN500 ISO-K flange (based on the design presented in [50]) allows for movements in the $\pm r$ direction without breaking the vacuum and with a resolution of ±1 mm.

All measurements are carried out at an RF power of 250 W, an argon pressure of 0.5 mTorr and a reflected power always less than 1%. Under these conditions, the plasma density peaks axially reaching a value of $\sim 10^{17}\,\mathrm{m}^{-3}$ to then decreases to $\sim 10^{16}\,\mathrm{m}^{-3}$ in the expansion chamber.

3. Results and discussion

Four different magnetic field strengths for the symmetric MN configuration were chosen, i.e. $B_{z,\mathrm{max}} = 77, 120, 175, 330$ G, and are denoted in the study as cases 'A', 'B', 'C' and 'D', respectively. The chosen fields correspond to four different ion magnetisation conditions under the antenna: (a) $r_{\mathrm{L,i}} \geqslant R$, (b) $r_{\mathrm{L,i}} \sim R$, (c) $r_{\mathrm{L,i}} < R$, and (d) $r_{\mathrm{L,i}} \ll R$, where $r_{\mathrm{L,i}}$ is the ion gyroradius and R is the plasma source inner radius. Assuming realistic upper and lower boundary values for T_i, i.e. 'cold' ions at room temperature and 'hot' ions with $T_\mathrm{i} = 800$ K, the ion gyro-radii on axis under the antenna are in the range of: $r_{\mathrm{L,i}}/R \approx 1 - 1.7$, $r_{\mathrm{L,i}}/R \approx 0.7 - 1.1$, $r_{\mathrm{L,i}}/R \approx 0.4 - 0.8$, and $r_{\mathrm{L,i}}/R \approx 0.2 - 0.4$. Recent studies observed that the level of ion magnetisation under the antenna could affect the transport of hot energetic electrons at the magnetic nozzle throat, and thus the plasma profile in the convergent part of the MN [31–33]. The magnetic field strengths chosen are used to study how the magnitude of $\boldsymbol{B}$ affects the plasma characteristics and whether the level of ion magnetisation under the antenna also affects the downstream plasma profile. It should be noted that for the axisymmetric MN configuration, the topology of the magnetic field lines stays invariant with increasing field strength, and that the deflected configuration is achieved solely by using the inner most solenoid. The magnetic field lines for the symmetric and steered magnetic nozzle can be seen in figure 3. The maximum magnetic field strength on axis in the deflected case is set to $B_{z,\mathrm{max}} = 330$ G to match the $B_{z,\mathrm{max}}$ obtained in the symmetric configuration (i.e. case D). The highest magnetic field case was chosen in order to maximise the magnetisation rate of the ions during the expansion.

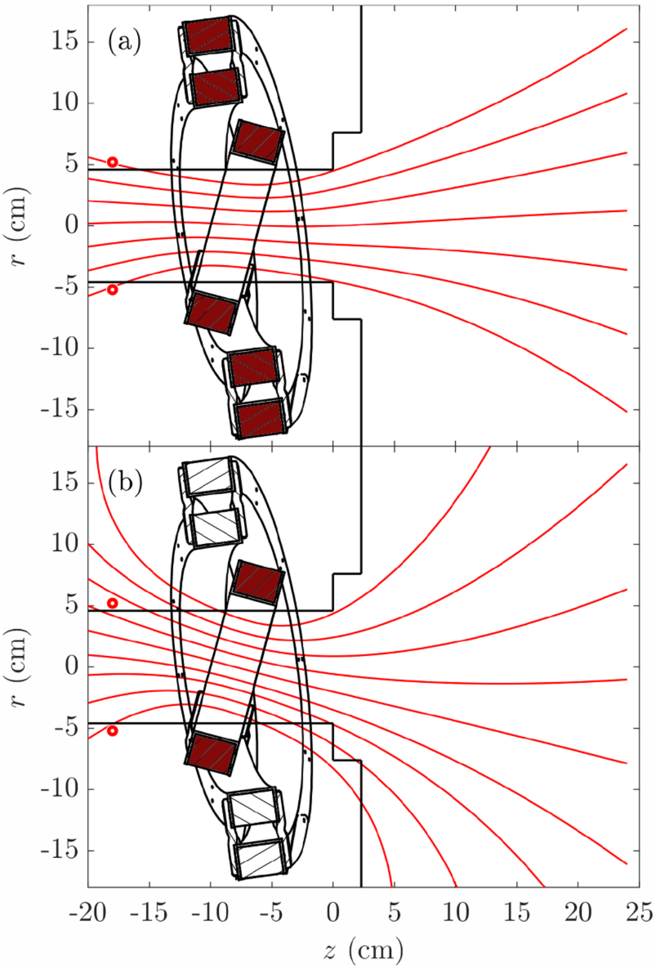

Figure 3. Magnetic field lines for the symmetric (a) and deflected (b) magnetic nozzle orientations. The section view of the coils on the r–z plane is also shown. The coils employed to achieve the analysed orientations are coloured in dark red.

3.1. Symmetric magnetic nozzle

Figure 4 shows the 2D mappings of the ion saturation current measured on axis in the plasma source with the planar LP for the different magnetic field cases. As expected, the ion saturation current increases on axis with increasing field strength. At very low magnetic fields (i.e. 77 G), I_sat peaks just after the antenna at $z = -15$ cm. As the magnetic field strength increases, the peak moves towards the magnetic nozzle throat and the maximum is at $z = -10$ cm. The transition between the I_sat peak under the antenna and I_sat peak closer to the solenoids centre seems to occur at the transition between unmagnetised ($r_{\mathrm{L,i}} \gtrsim R$) and magnetised ions ($r_{\mathrm{L,i}} < R$) under the antenna. This same behaviour has been observed experimentally by [31–33]. A possible explanation has been attributed to the influence of wall charging under the antenna on the transport of hot energetic electrons. It was observed that, as the magnetic field decreased, the increased ion flux to the insulating boundary due to the larger Larmor radii caused the glass tube

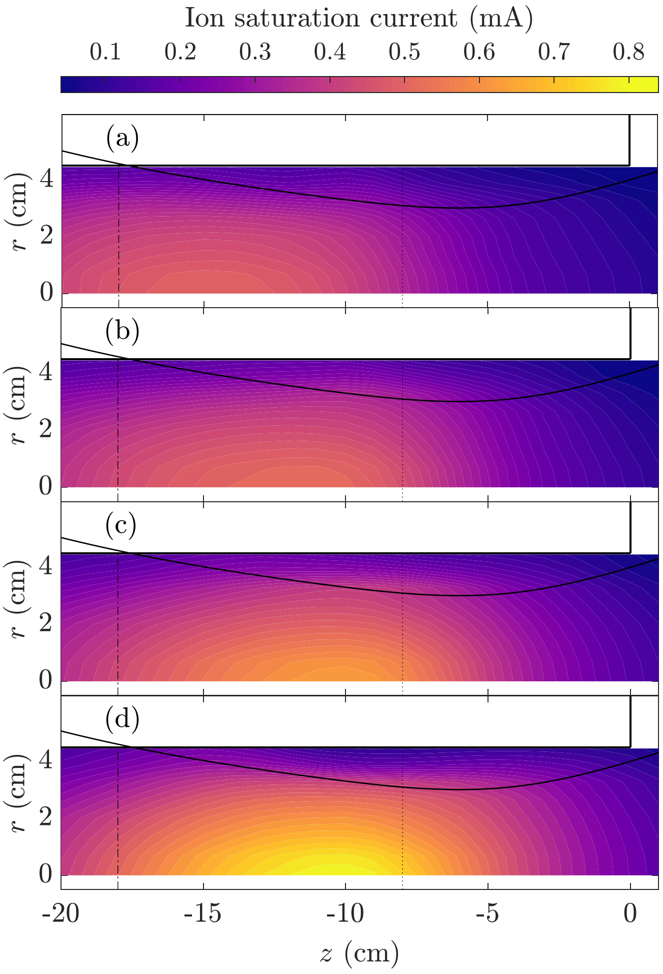

Figure 4. Ion saturation current contour plots measured in the plasma source for $B_{z,\max} = 77\,\mathrm{G}$ (a), $B_{z,\max} = 120\,\mathrm{G}$ (b), $B_{z,\max} = 175\,\mathrm{G}$ (c), and $B_{z,\max} = 330\,\mathrm{G}$ (d). The magnetic streamline that intersects the antenna is also shown in black. The dashed–dotted and dotted lines represent the position of the antenna and of the magnetic nozzle throat, respectively.

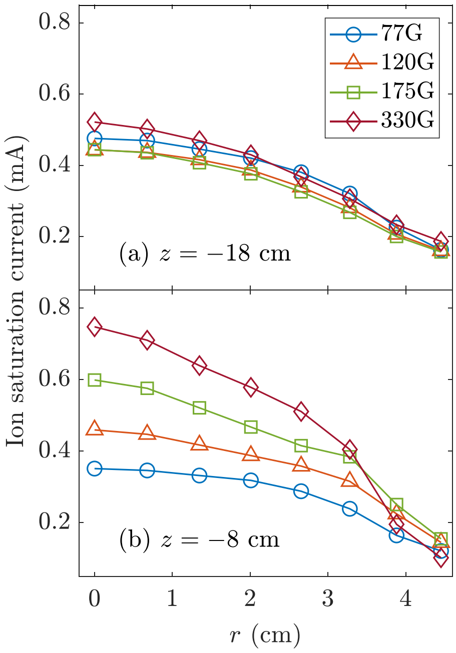

Figure 5. Ion saturation current measured radially under the antenna at $z = -18\,\mathrm{cm}$ (a) and under the solenoids at $z = -8\,\mathrm{cm}$ (b) for increasing magnetic field.

to charge more positively. As a consequence, a higher proportion of the energetic electrons generated some skin depths under the antenna would be electrostatically trapped, instead of being able to travel along the magnetic field lines and contribute to local ionisation at the magnetic nozzle throat.

Figure 5 shows the ion saturation current measured radially under the antenna (a) and under the solenoids (b). In both locations, I_{sat} always peaks on axis ($r = 0\,\mathrm{cm}$). Under the antenna (at $z = -18\,\mathrm{cm}$), increasing the magnetic field strength does not significantly affect the density profile, but it is worth noting that I_{sat} measured at the lowest magnetic field case (A) is slightly greater than for cases B and C, $0.48 \pm 0.005\,\mathrm{mA}$ vs $0.44 \pm 0.005\,\mathrm{mA}$. On the other hand, as it can be seen in figure 5(b), at the magnetic nozzle throat ($z = -8\,\mathrm{cm}$) the density increases with increasing magnetic field likely due to the reduced cross-field diffusion.

The profile of the measured ion saturation current in figure 5(b) can be explained by looking at the radial plasma potential profiles measured in the source with the emissive probe and shown in figure 6(c). Under the solenoids at $z = -8\,\mathrm{cm}$, the plasma potential peaks in the centre and then decreases radially for $B_{z,\max} = 77\,\mathrm{G}$ and $B_{z,\max} = 120\,\mathrm{G}$; thus, the outward diffusion of the ions is promoted. On the other hand, for the $B_{z,\max} = 175\,\mathrm{G}$ and $B_{z,\max} = 330\,\mathrm{G}$ cases, the plasma potential has a minimum in the centre. This profile translates into a potential well that would enhance ion confinement. Under the antenna (see figure 6(b)), V_{p} has a minimum at the source edge for all magnetic field cases. While for $B_{z,\max} = 330\,\mathrm{G}$ the profile dips at $r \approx 1\,\mathrm{cm}$, the other $\boldsymbol{B}$ cases present a potential drop at the same location i.e. $r \approx 4\,\mathrm{cm}$. As measured in similar experiments, the electron temperature profile in the plasma source showed an off-axis peak [16, 19, 20]. Due to the radial potential structure under the antenna, the high-temperature electrons created in the skin layer would tend to diffuse radially towards the axis. However, because an applied magnetic field is present, the cross-field diffusion of the electrons is reduced. For the magnetic field strengths studied, the electrons are well magnetised in the source and their gyroradius under the antenna is $r_{\mathrm{L,e}} \sim 0.5 - 4\,\mathrm{mm}$. Thus, the electrons with energies high enough to overcome the axial potential structure can be transported downstream along the peripheral field lines and contribute to local ionisation.

Figure 6(a) shows the plasma potential measured along the axis z. The emissive probe was used to map V_{p} in the source ($-23 < z < 3\,\mathrm{cm}$), while the plasma potential in the expansion chamber was measured with the RFEA ($3 < z < 19\,\mathrm{cm}$). The plasma potential structure on axis in the plasma source closely fits the Boltzmann relation $V_{\mathrm{p}}(z) = V_{\mathrm{p}}(z_0) + T_{\mathrm{e}} \ln\left[\frac{n_{\mathrm{i}}(z)}{n_{\mathrm{i}}(z_0)}\right]$ for $T_{\mathrm{e}} = 6\,\mathrm{eV}$, comparing well with measurements of the electron temperature done with the RFEA in electron collection mode (not reported here). An example of the plasma potential in the source obtained with the Boltzmann relation is shown by the

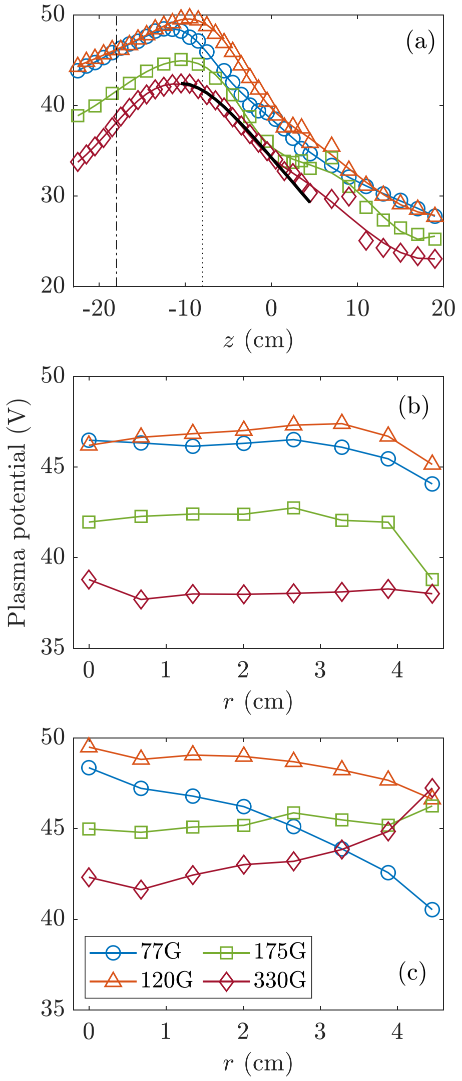

Figure 6. Plasma potential profiles measured (a) along the axis, (b) radially at the antenna axial position ($z = -18$ cm), and (c) radially at the solenoids axial position ($z = -8$ cm). The black solid line in (a) is the plasma potential obtained from the Boltzmann relation.

solid black line in figure 6(a). It is also noted that the locations of the peak potential agree well with the maxima of ion saturation current measured with the LP for all conditions. An ambipolar electric field, and not a current-free double-layer, seems to occur in the device, which is also reflected by the monotonic decrease in density along the axis. The electric field on axis for all four magnetic field cases is on average $\approx 0.5\,\mathrm{V\,cm^{-1}}$. Hence, the potential structure on axis is not substantially modified by the magnetic field strength.

Figure 7 shows contour plots of the ion saturation current measured in the expansion chamber with the planar Langmuir probe for increasing magnetic field strengths. The data has been mirrored for visual clarity, and is a good approximation of the actual profiles as previous full radial measurements showed a roughly symmetric conical structure around the axis. As can be seen, a hollow ion saturation current is present for all cases. The double-peaked structure becomes more prominent as the magnetic field strength is increased and, while for the lowest magnetic field cases (A and B) the profile starts to flatten out as it expands along the z axis, the data collected at higher field strengths show a significant hollow profile even beyond $z > 10$ cm. The onset of the high-density conics can be determined when the ratio of the maximum value of I_{sat} over I_{sat} measured on axis is bigger than one, i.e. $I_{\mathrm{sat},r}/I_{\mathrm{sat},0} > 1$. Figure 8 shows the radial profile of the ion saturation current measured at different axial locations and extrapolated from figure 7. As shown in figure 8(a), the profile peaks on axis for all magnetic field strengths just after the geometrical expansion interface, i.e. $z = 0$ cm. This profile mirrors the axially peaking I_{sat} measured in the source. However, moving along the axis, the conics start appearing further downstream and roughly at the same location for the higher magnetic field cases (B, C & D): for 120 G at $z > 5.5$ cm, for 175 G at $z > 7$ cm, and for 330 G at $z > 6$ cm. On the other

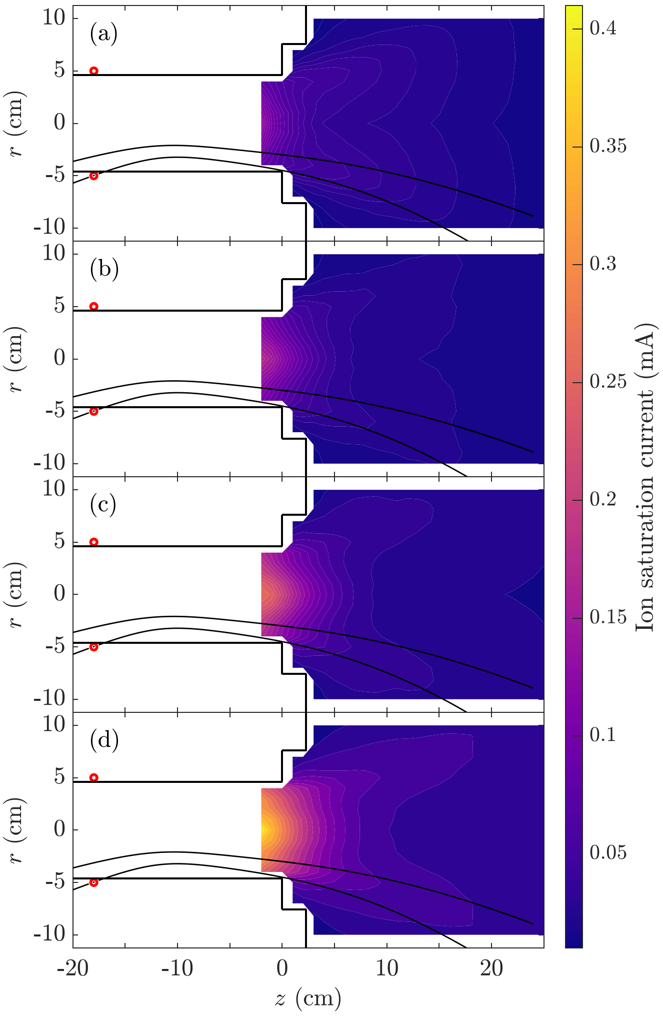

Figure 7. Ion saturation current contour plots measured in the expansion chamber for $B_{z,\max} = 77$ G (a), $B_{z,\max} = 120$ G (b), $B_{z,\max} = 175$ G (c), and $B_{z,\max} = 330$ G (d). The magnetic streamlines that encompass the peaks are also shown in black. The data has been mirrored for clarity.

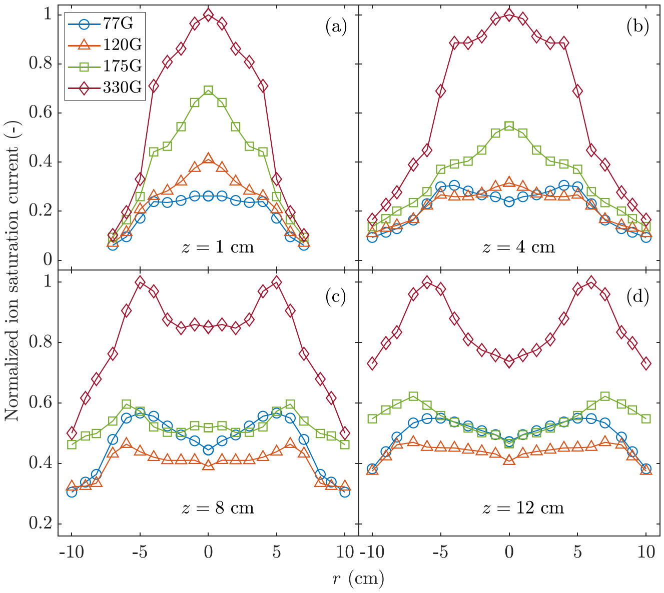

Figure 8. Radial profiles of the ion saturation current for increasing magnetic field strength measured downstream at different z locations. The values are normalised against the maximum value of I_{sat} at each z, and they have been mirrored for clarity.

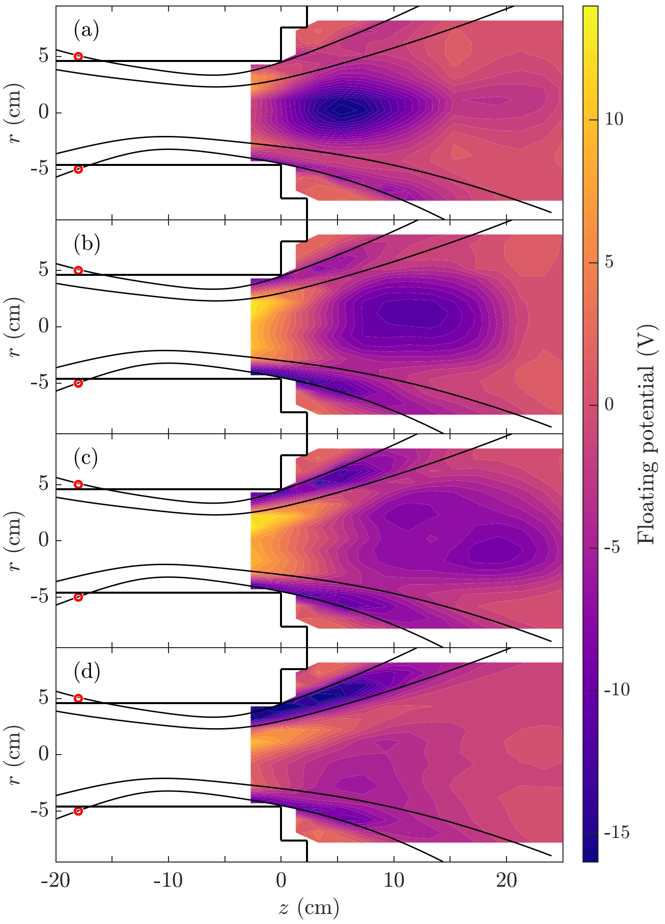

Figure 9. Floating potential contour plots measured in the expansion chamber for case A, $B_{z,\max} = 77$ G (a), case B, $B_{z,\max} = 120$ G (b), case C, $B_{z,\max} = 175$ G (c), and case D, $B_{z,\max} = 330$ G (d). The magnetic field lines that reconnect to the antenna are shown in solid black lines.

hand, at 77 G the conics appear closer to the source exit at $z > 2$ cm.

The field lines encompassing the conics are the most radial field lines that leave the source and intersect the antenna upstream, as observed in other experiments [13, 16, 18, 20]. The appearance of the hollow density structure has been attributed to the transport of high-energy electrons created under the antenna along these most radial field lines escaping the source and generating local ionisation [13, 15, 16, 19]. The presence of energetic electrons can be identified with large negative values of the floating potential V_{f} compared to the local plasma potential V_{p} [15, 43, 46, 51]. Figure 9 shows the spatial mappings of the floating potential measured in the expansion chamber for the different magnetic nozzle strengths analysed. A region of negative floating potential exists along the magnetic field lines that reconnect to the antenna for all cases, with V_{f} decreasing for higher field strengths. As discussed earlier, the electrons are restricted in their motion by the magnetic field, and their confinement in the peripheral regions improves as the magnetic field amplitude increases. This could explain the profile of V_{f} observed. This region matches well with the location of the conics occurrence in figure 7. It is also noted that figure 9(d) shows a more negative floating potential on the side that reconnects to the antenna feed ends (i.e. $r = +5$ cm), where $V_{\mathrm{f}} = -20$ V while $V_{\mathrm{f}} = -10$ V at $r = -5$ cm. This feature has also been reported by [46], and it could be caused by asymmetries due to instabilities in the conics region and/or non-uniform power deposition in the source [15, 23, 29].

An interesting feature of the spatial mappings shown in figure 9 is the presence of a region of negative V_{f} along the axis for $B_{z,\max} = 77$ G and $B_{z,\max} = 120$ G. In particular, figure 9(a) shows a significant negative potential ($V_{\mathrm{f}} = -16$ V) at $z \approx 6$ cm, and figure 9(b) has a peak of $V_{\mathrm{f}} = -11$ V at $z \approx 12$ cm. As can be seen in figure 9(c), data collected at $B_{z,\max} = 175$ G also suggests the presence of high-energy electrons on axis with a local maximum at $z \approx 19$ cm; however, higher values of floating potential are measured in the peripheral regions. The presence of energetic electrons on axis far from the antenna could be a sign of wave-heating mechanisms occurring at low magnetic fields. Measurements of the plasma resistance taken for increasing field magnitudes (not reported here) have shown a peak at the same magnetic field strengths, providing further interest into the study of helicon waves for cases A and B. However, a detailed analysis of wave propagation in the device is out of the scope of this research.

Figure 10 shows the radial profile of the local plasma potential measured in the expansion chamber at $z = 7$ cm with the RFEA. As shown in the plot, the plasma potential peaks on axis for all cases analysed and decreases radially. The ensuing electric field is on the order of ~ 1 V cm^{-1} and would result in a radial diffusion of the ions.

The hollow profile of I_{sat} described (shown in figure 8) has been reported by other studies [13, 16, 18, 20, 23, 24]. However, the structure observed in this experiment differs from previous work. Some have reported a conical profile

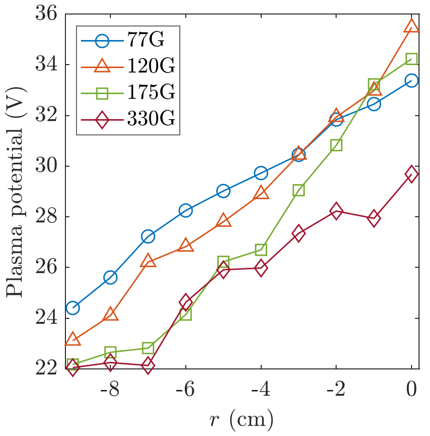

Figure 10. Radial profiles of the plasma potential measured in the expansion chamber at $z = +7\,\mathrm{cm}$.

that appears close to the antenna in the source and extends downstream [12, 24], others have measured islands of higher density appearing downstream with the peak density increasing axially along the peripheral regions [14, 18]. In our study, while the I_{sat} profiles peak on axis inside the source, the hollow structure forms downstream and the density decreases monotonically in the axial direction (see figures 5, 7 and 8). References [17, 20] have also observed the high-density conics forming downstream of the magnetic nozzle throat, with a centrally peaked density profile in the source.

A detailed and universally accepted explanation of the remote ionisation mechanism is still missing. The mean free path for electron-neutral ionisation collisions for the working pressures where conics have been observed is $\sim$1 m, which is of the same order or longer than the length of the experimental devices. Therefore, it has been argued that the probability of a high-energy electron ($\varepsilon > 15.8\,\mathrm{eV}$) impacting with a neutral atom while travelling on a linear path along the most radial field lines would be too low to explain the off-axis increase of density downstream the magnetic nozzle. Saha *et al* [14] explained the hollow density structure being generated by the cross-field diffusion that would cause a radial transport of the plasma at the edges, where ions were confined in a peripheral potential well (not observed here). Nevertheless, local ionisation was ruled out in that study since a peripheral high-energy electron tail was not detected. References [17, 20] attributed the enhanced off-axis ionisation to the drift caused by the strong radial gradient of the magnetic field in the expansion region that would allow electrons to cover a longer distance before hitting the experiment boundaries. In the apparatus presented here, the electrons drift speed in the azimuthal direction due to ∇B would be $v_{\mathrm{drift}} \sim 10^4\ \mathrm{m\ s^{-1}}$. However, it is noted that the thermal speed of electrons is of the order of $10^6\ \mathrm{m\ s^{-1}}$, meaning that the electrons would not be able to cover one rotation due to the drift motion before impacting the chamber walls.

Furthermore, contrary to what has been seen by [24], the conical structure appears in the device even when the ions are not magnetised in the antenna region ($B_{z,\mathrm{max}} = 77\,\mathrm{G}$). However, it is noted that the structure of the conics that occur for case A shows significant differences when compared to the other cases studied: (a) they appear much closer to the source exit, and (b) the downstream floating potential profile shows a significant minimum on axis when compared to the peripheral V_{f} measurements. An explanation for this discrepancy is still unclear and further studies are required to understand the dissimilar behaviour observed.

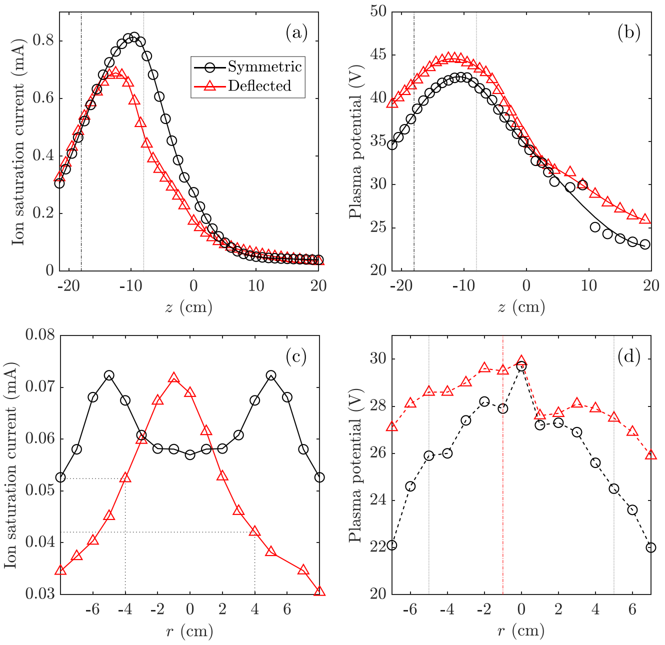

Figure 11. Ion saturation current (a) and plasma potential (b) measured on axis for the symmetric (black circles) and the deflected (red triangles) MN configurations. The dash-dotted and dotted line in (a) and (b) represent the axial location of the antenna and the coils centre, respectively. Ion saturation current (c) and plasma potential (d) plots measured radially at $z = 9\,\mathrm{cm}$. The data in (c) and (d) for the symmetric nozzle case has been mirrored for clarity.

3.2. Deflected magnetic nozzle

For this study, only the inner coil was employed to generate the non-symmetric magnetic field and allow the magnetic nozzle to deflect on the r–z plane. In this configuration, the magnetic nozzle is deflected by $\theta_{\mathrm{d}} = 15^\circ$, where θ_{d} is defined as the angle between the central magnetic field line and the z axis. It has to be noted that the current diagnostics system in the plasma source does not allow for measurements on the r–z plane, but only on the θ–z plane. Measurements are then translated into the r–z plane via trigonometry. This requires assuming that the plasma is cylindrical symmetric in the plasma source. However, this is not the case for the deflected nozzle case, and in the source only data on axis can be obtained. Thus, the 2D mappings reported in this section are solely collected in the expansion chamber. It has to be noted that this assumption might not be valid in the regions close to the antenna legs even for the symmetric magnetic nozzle configuration, where a non-uniform power deposition could occur.

Figure 11 shows the ion saturation current and plasma potential measured on axis, together with plots of I_{sat} and

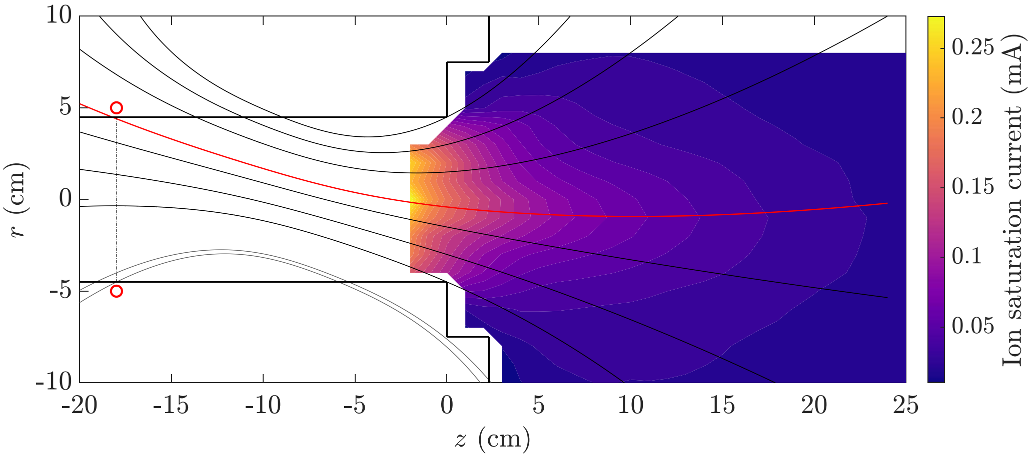

Figure 12. Contour plots of the ion saturation current measured in the chamber for the deflected MN configuration. The red line shows the magnetic field that crosses the antenna and leaves the source.

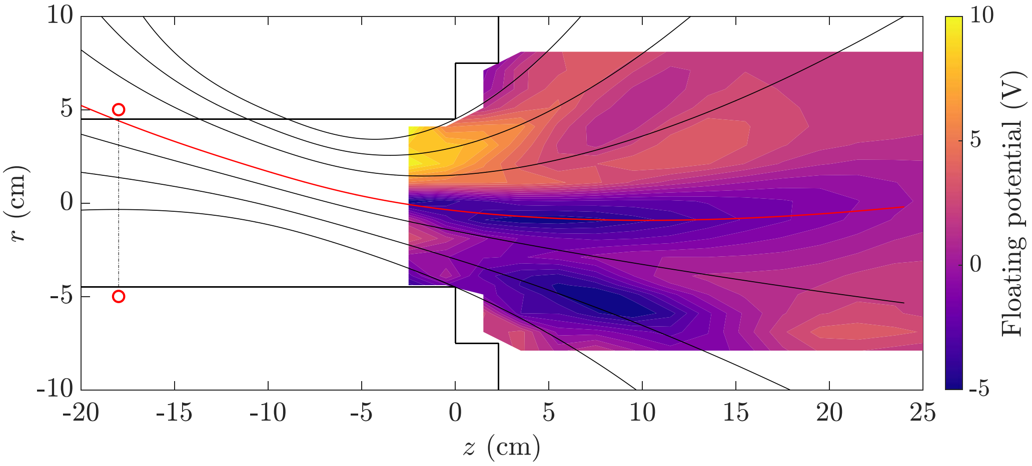

Figure 13. Contour plots of the floating potential measured in the chamber for the deflected MN configuration. The red line shows the magnetic field that crosses the antenna and leaves the source.

V_p measured radially downstream the nozzle throat. The red dash-dotted and black dotted lines in figure 11(d) represent the radial locations of the ion saturation current peaks measured at $z = 9$ cm and shown in figure 11(c). As seen in figure 11(a), the peak of I_sat on axis for the deflected case is closer to the antenna, i.e. at $z = -13$ cm, and the magnitude in the source region is lower compared to the symmetric case. The drop in the collected current for the deflected case can be attributed to an increased plasma loss to the source wall following the bent field lines. Similarly to the symmetric case, an axial electric field ($\approx 0.6\,\mathrm{V\,cm^{-1}}$) that would accelerate the ions downstream also occurs when an asymmetric magnetic field is present and is comparable to the one measured for the symmetric configuration ($\approx 0.5\,\mathrm{V\,cm^{-1}}$). Therefore, the bent field lines do not significantly affect the potential structure on axis. On the contrary, the radial profile of V_p measured downstream and shown in figure 11(d) differs for the two nozzle orientations. For the standard MN configuration, the plasma potential profile is, as expected, approximately symmetric with respect to the axis and peaks in the centre, showing a constant rate of potential drop of $\approx 1\,\mathrm{V\,cm^{-1}}$. However, the profile measured in the deflected nozzle is asymmetric. The potential structure in the negative r direction shows a plateau at $-2 < r < 0$ cm to then drop, while in the positive radial coordinates a drop of 2 V occurs in only $\Delta r = 1$ cm, and the plasma potential then decreases with increasing radial position.

Figures 12 and 13 show the contour plots of the ion saturation current and floating potential measured with the deflected magnetic nozzle configuration, respectively. As seen in figure 12, the I_sat profile does not exhibit a double-peaked profile, but rather a single peak centred at $r = -1$ cm that expands downstream. By looking at a slice of the 2D plot in figure 11(c), it is observed that the radial profile of I_sat is not symmetric with respect to the axis (i.e. $r = 0$ cm), but rather it shows greater values in the $-r$ direction (see dotted black lines for clarity). Thus, the plasma density would be higher in the negative radial region, which is in the direction of the magnetic nozzle orientation. It is interesting to note that, while the magnetic nozzle was deflected by $\theta = 15^\circ$, the location of the I_sat peak is shifted only $\approx 4^\circ$ from the z axis.

A possible explanation for the double-peak to single-peak profile transition could be the non-uniformity of the magnetic field in the plasma source. Some of the high energy electrons created under the antenna in the region $r \approx -4.5\,\text{cm}$ will be directly lost to the source walls following the bent streamlines (grey lines in figure 12), thereby inhibiting their escape from the plasma source into the chamber.

The striking feature of the contour plot in figure 12 is the location of the maximum ion saturation current which corresponds to the streamline that reconnects to the antenna in the plasma source and matches the plateau of plasma potential shown in figure 11(d). By analysing the floating potential profile in figure 13, a negative potential region is present precisely on the same streamline. The same feature has been measured for the symmetric magnetic nozzle case, even if the plasma density profile in the expansion chamber differs remarkably for the two orientations. It is also worth noting that when analysing the radial profile of the floating potential measured for example at $z = 9\,\text{cm}$, a step drop of V_f occurs around the axis, which is reversed compared to the profile of V_p in figure 11(d) (i.e. lower values of V_f for $r < 0\,\text{cm}$ and higher V_f for $r > 0\,\text{cm}$). This could be an additional sign of the presence of high-energy electrons solely in the negative radial region. Thus, the data strongly suggest that the local plasma characteristics are dictated by the magnetic field lines that intersect the antenna and expand downstream independently of the field strength and orientation, and transporting alongside the free population of high-energy electrons created in the source.

Figure 13 also shows a second region of negative floating potential centred at $(r,z) = (-5,8)$ which is currently not understood and is the focus of future studies. However, it is interesting to consider the direction of the central magnetic field line in the asymmetric nozzle case. At $z = 8\,\text{cm}$, the central field line that is deflected by $\theta_\text{def} = 15^\circ$ has a radial coordinate of $r = -4.3\,\text{cm}$, which approximately coincides with the second minimum of V_f measured at $(r-z) = (-5,8)\,\text{cm}$. Further measurements are required to better understand the nature of this second minima of V_f.

4. Conclusion

In this work, the effect of magnetic field strength and orientation on a RF plasma device where the plasma is created far from the magnetic nozzle throat has been studied. Four different magnetic field strengths were analysed for the symmetric magnetic nozzle configuration. While the ion saturation current peaks on axis in the plasma source, a double-peaked hollow I_sat profile forms downstream the MN throat for all the cases studied, which expands along the most radial field lines intersecting the antenna and leaving the source. Thus, contrary to what has been observed in the plasma source, the level of ion magnetisation under the antenna appears not to influence the formation of the radially peaking I_sat profile downstream the MN. It is also observed that the high-density conics structure becomes more prominent with increasing magnetic field strength. The spatial measurements also allowed the observation of how the axial location of the conics changes in response to the magnetic field strength. Negative regions of floating potential, which can be associated with the presence of high-energy electrons, match the location of maximum I_sat regions. At higher magnetic field strengths, the floating potential becomes more negative in the peripheral region corresponding to the magnetic field lines that reconnect to the antenna. This further supports the hypothesis that the population of free high-energy electrons is responsible for the generation of the peripheral high-density profile. Additionally, in the symmetric nozzle case, V_f shows a more negative region along the axis for the lowest field strength cases and is currently attributed to wave-heating mechanisms; however, future B-dot measurements are necessary to measure the possible presence of helicon waves.

With the deflected magnetic nozzle configuration, the high-density conics disappear downstream, and the ion saturation current peaks at $r = -1\,\text{cm}$. At the same radial location, a minimum of the floating potential is also measured. As observed for the symmetric MN case, both the maximum of I_sat and the negative region of V_f occur on the field line that connects to the antenna, which is further evidence of how the magnetic field lines interacting in the source affect the local plasma characteristics downstream of the MN. Furthermore, a higher ion saturation current was observed in the negative radial region following the magnetic nozzle deflection.

A complete understanding of the mechanisms that drive remote ionisation in the experiment presented is still unclear. Future work is necessary to map electron energy probability functions and correlate the high-energy electron densities with ionisation rates to better understand how remote ionisation could happen over a distance significantly shorter than the electron-neutral collision mean-free path. However, this study demonstrates how the magnetic field topology, and particularly the field lines that cross the antenna and can expand freely in the expansion region, affect the plasma characteristics downstream the magnetic nozzle.

Data availability statement

The data that support the findings of this study are available from the corresponding author upon reasonable request. All data that support the findings of this study are included within the article (and any supplementary files).

Acknowledgments

The research was mainly supported by the Asian Office of Aerospace Research and Development (AOARD), the international office of the Air Force Office of Scientific Research (AFOSR), under Grant Number #FA2386-19-1-4012. The authors declare that the research was conducted in the absence of any commercial or financial relationships that could be construed as a potential conflict of interest.

ORCID iDs

A Caldarelli https://orcid.org/0000-0002-0230-162X
J E Cater https://orcid.org/0000-0002-3233-4000

References

[1] Lieberman M A and Lichtenberg A J 2005 *Principles of Plasma Discharges and Materials Processing* (New York: Wiley) pp 165–206

[2] Block L P 1978 A double layer review *Astrophys. Space Sci.* **55** 59–83

[3] Yamada M, Kulsrud R and Ji H 2010 Magnetic reconnection *Rev. Mod. Phys.* **82** 603–64

[4] Charles C and Boswell R 2003 Current-free double-layer formation in a high-density helicon discharge *Appl. Phys. Lett.* **82** 1356–8

[5] Charles C *et al* 2006 Helicon double layer thruster *Collection of Technical Papers—AIAA/ASME/SAE/ASEE 42nd Joint Propulsion Conf.* vol 7

[6] Charles C and Boswell R W 2004 Laboratory evidence of a supersonic ion beam generated by a current-free 'helicon' double-layer *Phys. Plasmas* **11** 1706–14

[7] Cox W, Charles C, Boswell R W and Hawkins R 2008 Spatial retarding field energy analyzer measurements downstream of a helicon double layer plasma *Appl. Phys. Lett.* **93** 071505

[8] Ahedo E and Navarro-Cavallé J 2013 Helicon thruster plasma modeling: two-dimensional fluid-dynamics and propulsive performances *Phys. Plasmas* **20** 043512

[9] Lafleur T 2014 Helicon plasma thruster discharge model *Phys. Plasmas* **21** 043507

[10] Bennet A, Charles C and Boswell R 2018 *Insitu* electrostatic characterisation of ion beams in the region of ion acceleration *Phys. Plasmas* **25** 023516

[11] Takahashi K 2019 Helicon-type radio-frequency plasma thrusters and magnetic plasma nozzles *Rev. Mod. Plasma Phys.* **3** 044510

[12] Takahashi K 2022 Thirty percent conversion efficiency from radio-frequency power to thrust energy in a magnetic nozzle plasma thruster *Sci. Rep.* **12** 18618

[13] Charles C 2010 High density conics in a magnetically expanding helicon plasma *Appl. Phys. Lett.* **96** 051502

[14] Saha S K, Chowdhury S, Janaki M S, Ghosh A, Hui A K and Raychaudhuri S 2014 Plasma density accumulation on a conical surface for diffusion along a diverging magnetic field *Phys. Plasmas* **21** 043502

[15] Gulbrandsen N and Fredriksen Å 2017 RFEA measurements of high-energy electrons in a helicon plasma device with expanding magnetic field *Front. Phys.* **5** 2

[16] Takahashi K, Akahoshi H, Charles C, Boswell R W and Ando A 2017 High temperature electrons exhausted from RF plasma sources along a magnetic nozzle *Phys. Plasmas* **24** 084503

[17] Ghosh S, Yadav S, Barada K K, Chattopadhyay P K, Ghosh J, Pal R and Bora D 2017 Formation of annular plasma downstream by magnetic aperture in the helicon experimental device *Phys. Plasmas* **24** 020703

[18] Bennet A, Charles C and Boswell R 2018 Selective radial release of hot, magnetised electrons downstream of a low-pressure expanding plasma *J. Phys. D: Appl. Phys.* **51** 375204

[19] Bennet A, Charles C and Boswell R 2018 Separating the location of geometric and magnetic expansions in low-pressure expanding plasmas *Plasma Sources Sci. Technol.* **27** 075003

[20] Yadav S, Ghosh S, Bose S, Barada K, Pal R and Chattopadhyay P 2018 Role of ion magnetization in formation of radial density profile in magnetically expanding plasma produced by helicon antenna *Phys. Plasmas* **25** 043518

[21] Takahashi K, Sugawara T and Ando A 2020 Spatial measurement of axial and radial momentum fluxes of a plasma expanding in a magnetic nozzle *New J. Phys.* **22** 073034

[22] Buschmann L and Fredriksen Å 2022 Axial and radial development of the hot electron distribution in a helicon plasma source, measured by a retarding field energy analyzer (RFEA) *Plasma Sources Sci. Technol.* **31** 025005

[23] Caldarelli A, Filleul F, Charles C, Boswell R W, Rattenbury N and Cater J 2022 Radial characterization of an ion beam in a deflected magnetic nozzle *J. Electr. Propuls.* **1** 10

[24] Emoto K, Takahashi K and Takao Y 2023 Density profile transition and high-energy electron transport in a magnetically expanding radio frequency plasma *Phys. Plasmas* **30** 013509

[25] Boswell R W, Takahashi K, Charles C and Kaganovich I D 2015 Non-local electron energy probability function in a plasma expanding along a magnetic nozzle *Front. Phys.* **3** 14

[26] Akahoshi H, Takahashi K and Ando A 2018 Filtering peripheral high temperature electrons in a cylindrical RF-driven plasmas by an axisymmetric radial magnetic field *AIP Adv.* **8** 035208

[27] Cox W, Charles C, Boswell R W, Laine R and Perren M 2010 Magnetic ion beam deflection in the helicon double-layer thruster *J. Propuls. Power* **26** 1045–52

[28] Merino M and Ahedo E 2017 Contactless steering of a plasma jet with a 3D magnetic nozzle *Plasma Sources Sci. Technol.* **26** 095001

[29] Imai R and Takahashi K 2022 Deflections of dynamic momentum flux and electron diamagnetic thrust in a magnetically steered RF plasma thruster *J. Phys. D: Appl. Phys.* **55** 135201

[30] Takahashi K and Imai R 2022 Two-dimensional deflection of a plasma plume exhausted from a magnetically steered radio-frequency plasma thruster *Phys. Plasmas* **29** 054501

[31] Bennet A, Charles C and Boswell R 2019 Non-local plasma generation in a magnetic nozzle *Phys. Plasmas* **26** 072107

[32] Filleul F, Caldarelli A, Charles C, Boswell R W, Rattenbury N and Cater J 2021 Characterization of a new variable magnetic field linear plasma device *Phys. Plasmas* **28** 123514

[33] Filleul F, Caldarelli A, Boswell R W, Charles C, Rattenbury N and Cater J 2022 The role of ion magnetization on plasma generation in a magnetic nozzle RF device *J. Electr. Propuls.* **1** 20

[34] Takahashi K, Charles C and Boswell R W 2022 Wave-driven electron inward transport in a magnetic nozzle *Sci. Rep.* **12** 20137

[35] Takahashi K, Takao Y and Ando A 2018 Thrust imparted by a stepped-diameter magnetic nozzle RF plasma thruster *Appl. Phys. Lett.* **113** 034101

[36] Sumikawa S and Takahashi K 2023 Radial profile control of a magnetically expanding plasma and its impact on a plasma thruster *Jpn. J. Appl. Phys.* **62** SL1001

[37] Sheehan J P and Hershkowitz N 2011 Emissive probes *Plasma Sources Sci. Technol.* **20** 063001

[38] Sheehan J P, Raitses Y, Hershkowitz N and McDonald M 2017 Recommended practice for use of emissive probes in electric propulsion testing *J. Propuls. Power* **33** 614–37

[39] Böhm C and Perrin J 1993 Retarding field analyzer for measurements of ion energy distributions and secondary electron emission coefficients in low pressure radio frequency discharges *Rev. Sci. Instrum.* **64** 31–44

[40] Zhang Y, Charles C and Boswell R 2016 Effect of radial plasma transport at the magnetic throat on axial ion beam formation *Phys. Plasmas* **23** 083515

[41] Caldarelli A, Filleul F, Boswell R W, Charles C, Rattenbury N J and Cater J E 2023 Data processing

techniques for ion and electron-energy distribution functions *Phys. Plasmas* **30** 040501

[42] Keesee A M, Scime E E, Charles C, Meige A and Boswell R 2005 The ion velocity distribution function in a current-free double layer *Phys. Plasmas* **12** 093502

[43] Charles C and Boswell R 1995 Effect of wall charging on an oxygen plasma created in a helicon diffusion reactor used for silica deposition *J. Vac. Sci. Technol.* **13** 2067–73

[44] Charles C 2004 Hydrogen ion beam generated by a current-free double layer in a helicon plasma *Appl. Phys. Lett.* **84** 332–4

[45] Aanesland A, Charles C, Lieberman M A and Boswell R W 2006 Upstream ionization instability associated with a current-free double layer *Phys. Rev. Lett.* **97** 075003

[46] Takahashi K, Igarashi Y and Fujiwara T 2010 Plane and hemispherical potential structures in magnetically expanding plasmas *Appl. Phys. Lett.* **97** 041501

[47] Takahashi K, Charles C, Boswell R W and Fujiwara T 2010 Double-layer ion acceleration triggered by ion magnetization in expanding radio-frequency plasma sources *Appl. Phys. Lett.* **97** 10

[48] Lafleur T, Charles C and Boswell R W 2011 Electron temperature characterization and power balance in a low magnetic field helicon mode *J. Phys. D: Appl. Phys.* **44** 185204

[49] Zhang Y, Charles C and Boswell R 2016 Thermodynamic study on plasma expansion along a divergent magnetic field *Phys. Rev. Lett.* **116** 025001

[50] Cox W 2010 Magnetic steering of the ion beam in the helicon double layer thruster *PhD Thesis* The Australian National University The Australian National University

[51] Igarashi Y, Takahashi K and Fujiwara T 2011 Energetic electrons moving along peripheral magnetic field lines in magnetically expanding plasmas *IEEE Trans. Plasma Sci.* **39** 2442–3